

Morphological Redshift Estimates for Galaxy Clusters in a Sunyaev-Zel’dovich Effect Survey

J.M. Diego¹, J. Mohr², J. Silk¹, and G. Bryan¹.

¹*Astrophysics Dept. University of Oxford. Denys Wilkinson building. 1, Keble Road, Oxford OX1 3RH, UK*

²*Departments of Astronomy and Physics, University of Illinois, Urbana, IL 61801.*

draft

ABSTRACT

We develop a new method to estimate the redshift of galaxy clusters through resolved images of the Sunyaev-Zel’dovich effect (SZE). Our method is based on morphological observables which can be measured by actual and future SZE experiments. We test the method with a set of high resolution hydrodynamical simulations of galaxy clusters at different redshifts. Our method combines the observables in a principal component analysis. After *calibrating* the method with an independent redshift estimation for some of the clusters, we show—using a Bayesian approach—how the method can give an estimate of the redshift of the galaxy clusters. Although the error bars given by the morphological redshift estimation are large, it should be useful for future SZE surveys where thousands of clusters are expected to be detected; a first preselection of the high redshift candidates could be done using our proposed morphological redshift estimator. Although not considered in this work, our method should also be useful to give an estimate of the redshift of clusters in X-ray and optical surveys.

Key words: galaxies:clusters:general, methods: statistical

1 INTRODUCTION

The advent of new experiments dedicated to the observation of the Sunyaev-Zel’dovich effect (Sunyaev & Zel’dovich, 1972) (SZE hereafter), demands the development of new techniques to best analyze these new and exciting data. With the SZE it is possible to probe the hot plasma in galaxy clusters, which shifts the spectrum of the cosmic background radiation. This shift is redshift independent, and it is proportional to the temperature of the plasma and its electron density (n_e). This characteristic (z -independent, and $\propto n_e$) makes the SZE an ideal way to explore the high redshift population of galaxy clusters.

However, the fact that the SZE distortion is independent of the redshift of the cluster makes the determination of the redshift of the cluster a challenging task. Redshift information is crucial if one attempts to use cluster surveys to study the evolution of our universe. The evolution of the cluster number counts (dN/dz) is a very sensitive indicator of the cosmological model (Eke et al. 1998; Mathiesen & Evrard 1998; Henry 2000). The local abundance of clusters shows a degeneracy in $\Omega - \sigma_8$ (Eke et al. 1996; Bahcall et al. 1997) but this degeneracy can be broken with an accurate estimation of dN/dz up to moderate or high redshifts ($z \approx 0.5 - 1$) (see e.g. Bahcall & Fan 1998; Borgani et al. 2001). The cluster redshift distributions in suitably large SZE cluster surveys can potentially provide

precise constraints on the amount and nature of the dark energy in the universe (Haiman et al. 2001; Holder et al. 2001; Weller et al. 2001; Majumdar & Mohr 2002). Redshifts are also necessary to study the evolution of the cluster structure and dynamics.

One normally determines the redshift using photometric and spectroscopic observations of the galaxies in the cluster. Spectroscopic observations of galaxies in relatively nearby clusters are straightforward, but for distant clusters it is challenging even with the largest telescopes. For large solid angle surveys, photometric redshifts will be of critical importance, allowing redshift determination for far less time invested at the telescope. However, photometric redshifts are also time consuming and for clusters above redshift ≈ 1 , photometric redshifts require large telescopes (see for instance Diego et al. 2002 where the authors show the selection function for a galaxy cluster survey with a 10-m telescope and photometric redshift estimations). Future SZE experiments will detect hundreds and perhaps thousands of galaxy clusters. The *Planck* Surveyor SZE survey is expected to detect more than 10^4 clusters with redshifts extending to ~ 2 (depending on the cosmological model, Diego et al. 2002). A planned, arcminute resolution SZE survey from the South Pole will detect similar numbers of clusters with a much larger fraction at high redshift.

Measuring redshifts for large solid angle, high redshift

cluster surveys is a daunting task. An optimal solution may be to combine small and medium-sized telescopes to determine the redshifts of the low and intermediate z clusters, reserving the redshift measurements of the most distant clusters for the largest available telescopes. Clearly this strategy requires crude *a priori* knowledge of the cluster redshifts. The motivation of the work described here is to examine whether it is possible to make this preselection of the low, intermediate and high redshift clusters using SZE data alone.

Our method is based only on observed SZE properties of galaxy clusters. These include the observed shape and size of the cluster, which do have some dependence on the redshift. For instance, the apparent size of a particular cluster will decrease when increasing its redshift. So, an apparent size will, in principle, constrain the cluster redshift. However, the apparent size of the cluster also depends on its total mass. Two clusters with different redshifts and masses can have the same apparent size, provided the more distant cluster has a larger mass that exactly compensates for the decrease in the apparent size due to the increased redshift. There is, therefore, a degeneracy between the cluster redshift and mass.

The question is whether we can break this degeneracy by using additional information. A resolved SZE image of a cluster provides information not only about the cluster size, but also about the shape of the cluster gas distribution. The total observed flux of the cluster, for instance, depends on the total cluster mass, the redshift and the temperature. The central SZE decrement depends on the core radius and the electron central density, but it is, in principle, independent of the redshift. Our method incorporates these and other observables to break the mass–redshift degeneracy. This method requires resolved SZE images. Therefore, it should be useful for arcmin and sub-arcmin resolution experiments but not for experiments like *Planck*, where the best resolution will be 5 arcmin.

In this work we will not consider the effects of the relativistic corrections and the kinematic effect, because they are small compared with the non-relativistic thermal SZE. Their effect will be discussed in a later paper. In §2 we outline the connections between cluster morphology and redshift from a structure formation viewpoint. §3 discusses some of the weaknesses of this theoretical perspective and then provides a detailed description of a method that overcomes these weaknesses. A demonstration of the degree to which the method works is contained in §4, and a discussion of conclusions follows in §5.

2 CONNECTIONS BETWEEN CLUSTER MORPHOLOGIES AND REDSHIFTS

In this section we will use theoretical arguments to justify the use of morphological redshifts. We will develop a simple analytic cluster SZE model and then use it to compute cluster observables. For the particular case of the isothermal β -model in a cosmological model with $\Omega_m = 1$, we will demonstrate in subsection 2.2 how combined measurements of cluster size and flux lead directly to a redshift estimate. Although this cosmological model is not consistent with cur-

rent data, its simplicity make it useful for illustrating the method, and the results are fully generalizable.

2.1 A Model for Cluster SZE Signatures

The distortion in the CMB intensity due to thermal SZE is

$$\Delta I = I_o * f(x) * y_c \quad (1)$$

where $I_o \approx 2.7 \times 10^{11} \frac{mJy}{sr}$, x is the adimensional frequency ($x = h\nu/k_b T \approx \nu(GHz)/56.8$), $f(x)$ is the frequency dependence of the SZE $f(x) = [x \coth(x/2) - 4] \times [x^4 e^x / (e^x - 1)^2]$ and y_c is the cluster Compton parameter:

$$y_c = \frac{k_b \sigma_T}{m_e c^2} \int T n(l) dl. \quad (2)$$

This distortion is independent of cluster redshift because x does not depend on the redshift (because both ν and T depend on the redshift in the same way). Therefore, the SZE spectral distortion provides no redshift information about the cluster.

However, if we can produce a resolved SZE image of a cluster, we gain much more information and can potentially solve for the redshift. To illustrate this point, let us assume the simple case of a cluster at redshift z with an electron density profile described by a β -model (Cavaliere & Fusco-Femiano 1978) with $\beta = 2/3$, which is the value found to best match clusters (Jones & Forman 1984; Mohr et al. 1999). In this case the electron density profile is just $n(r) = n_o / (1 + (r/r_c)^2)$, where n_o is the electron central density and r_c is the core radius, which we take to be some constant fraction of the virial radius $r_c = r_v/p$. p is a parameter with value ranging between 10 and 20. More realistic modelings that included, for example, a mass dependent p , could be considered, but for illustrative purposes our simple model will suffice.

The redshift evolution of these parameter can be modeled as

$$n_o = N_o \frac{\Delta_c(z)}{\Delta_c(0)} E^2(z) \quad (3)$$

where $\Delta_c(z)$ is the critical collapse overdensity with respect to the critical density at redshift z ($\Delta_c(z) = 18\pi^2 + 82x - 39x^2$ with $x = \Omega(z) - 1$ and $\Omega(z) = \Omega_m(1+z)^3/E(z)^2$) and $H(z) = H_o E(z)$ (see e.g. Bryan & Norman 1998; Mohr et al. 2000). N_o is adjusted to fix the total gas mass $M_{gas} = \mu_e m_p \int_0^{r_v} n(r) 4\pi r^2 dr \approx f_b M$ where M is the virial mass and f_b is the baryon fraction. For a fully ionized, purely hydrogen gas $\mu_e = 1$. Similarly, for the virial radius we have

$$r_v = R_o M^{1/3} \left(\frac{\Delta_c(z)}{\Delta_c(0)} E(z)^2 \right)^{-1/3}. \quad (4)$$

Using the virial theorem ($2K + V = 0$) and the spherical collapse model, we can obtain an expression for the virial temperature of the cluster.

$$T = T_o M_{15}^{2/3} \left(\frac{\Delta_c(z)}{\Delta_c(0)} E(z)^2 \right)^{1/3}. \quad (5)$$

The normalization, T_o can be obtained from models or from a fit of this relation to the data. We will adopt the second approach and use the values derived in (Diego et al. 2001).

Within this model, the Compton parameter in the direction θ is

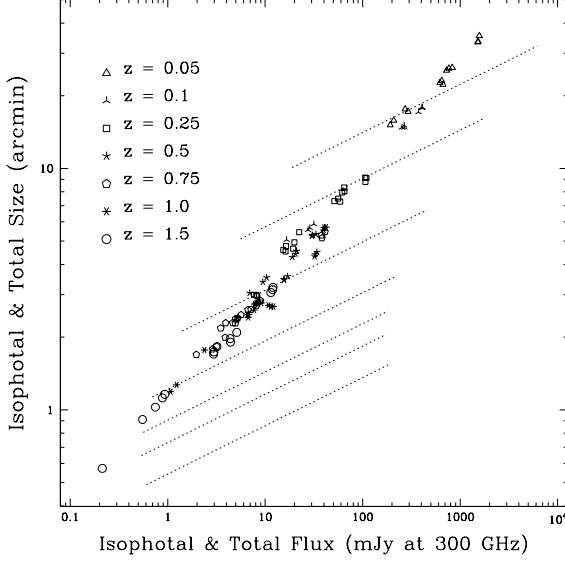


Figure 1. Ideal vs real case. The dotted lines represent the expected cluster total size-flux relation in the ideal case where the cluster is observed with infinite resolution and sensitivity. Each line corresponds to a different redshift (listed on the left) for a range of masses $3 \times 10^{13} - 1 \times 10^{15} h^{-1} M_{\odot}$. Top line is for $z = 0.05$ while bottom line is for $z = 1.5$. The symbols show the case in *real life* (simulations) where one observes isophotal quantities and the scaling relations differ from the case of the toy model. Note that in this case, the characteristic mass as a function of redshift for the simulated clusters is decreasing with redshift. This, and the fact that we are measuring isophotal sizes instead of virial sizes, explains the shift to the left with redshift.

$$y_c(\theta) = \frac{k_b \sigma_T}{m_e c^2} r_c n_o T \Phi(\theta) = y_o \Phi(\theta) \quad (6)$$

where θ is the angle between the line of sight and the center of the cluster. We have assumed here that T is constant, and we have ignored any contributions to the y_c from outside the cluster virial region. The function $\Phi(\theta)$ is just the integral of the density profile along the line of sight.

$$\Phi(\theta) = \frac{2}{\sqrt{1 + (\theta/\theta_c)^2}} \tan^{-1} \sqrt{\frac{p^2 - (\theta/\theta_c)^2}{1 + (\theta/\theta_c)^2}} \quad (7)$$

θ_c is the apparent core radius r_c/d_A . The cluster surface brightness profile is then

$$B(\theta) = B_o r_c n_o T \Phi(\theta) \quad (8)$$

where (see Eqn 1) $B_o = I_o f(x) (k_b \sigma_T / m_e c^2)$. Using this model we will now show how cluster morphologies contain information about the cluster redshift.

2.2 Redshifts from Total Flux and Apparent Size in the $\Omega = 1$ Case.

We now apply the model developed above to demonstrate that in principle two simple observables provide enough information to estimate cluster redshifts. We specifically use the evolution model appropriate for $\Omega_M = 1$ only for simplicity. In this simple case, the general expressions in the pre-

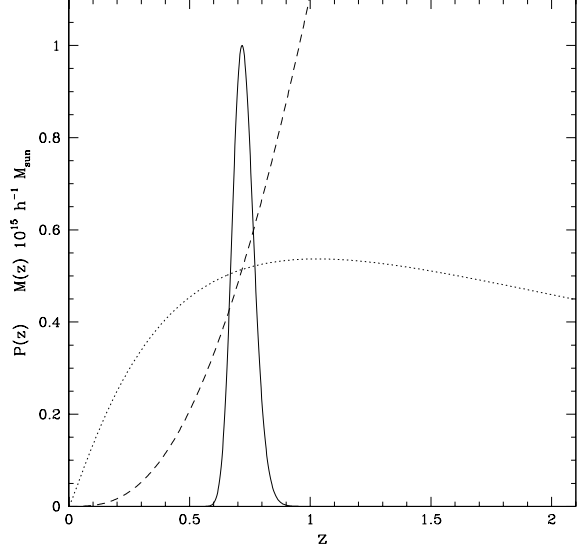


Figure 2. The ideal case. If the clusters follow exactly the scaling relations of equations (9) and (10), then the recovered redshift could be as good as the one shown in this figure. The solid line shows the Gaussian pdf of the recovered redshift for an experiment with 10 arcsec FWHM. In the computation of the pdf we have assumed that the flux is measured with no error and the diameter has an uncertainty given by the FWHM of the experiment. The dotted line is the mass as a function of redshift for a given flux, and the dashed line is the same for a given diameter. This plot is for a cluster with an apparent radius of 4 arcmin and a total flux of 100 mJy (at 353 GHz).

vious section reduce their complexity since $\Delta_c(z) = \Delta_c(0) = 18\pi^2$ and $E(z)^2 = (1+z)^3$.

The total cluster flux is just the integral of the SZE distortion or surface brightness over the entire solid angle of the cluster. $S = \int B(\theta) d\Omega$. Taking a step back and noting that the surface brightness is a line integral, it is clear that the total SZE flux is simply an integral over the cluster volume. Writing the volume element $dV(z) = d\Omega d_A(z)^2 dl$, where d_A is the angular diameter distance, we then show that $S = \int d\Omega \int dl T n = d_A^{-2} \int dV T n \propto \bar{T} M_{gas} d_A^{-2}$. The total cluster flux is an interesting quantity, depending on the density weighted temperature \bar{T} , the total gas mass (but not its detailed distribution) and the cluster distance. In the isothermal case the total flux at the frequency x is $S(x) = S_o (f_b T M_{15}) / d_A^2$, where $S_o \approx 3.781 \times f(x)$ mJy. We take the baryon fraction to be consistent with SZE observations ($f_b \approx 0.08 h^{-1}$ Grego et al. 2001). The mass M_{15} is expressed in units of $10^{15} h^{-1} M_{\odot}$. In these units, the h^{-2} dependence of d_A^2 is cancelled with the h -dependence of f_b and M_{15} making the flux h -independent. If we substitute mass for temperature (equation 5), we end up with an expression which only depends on the mass and the redshift.

$$S = \frac{S_o T_o f_b M_{15}^{5/3} (1+z)}{d_A^2} \quad (9)$$

The total flux of the cluster depends on its redshift through the angular diameter distance and inherent evolution of cluster structure.

The apparent size of the cluster θ_{cl} is another quantity which strongly depends on the cluster redshift. If we consider that the physical size of the cluster is related to its virial radius, then its observed apparent size is (see Eqn. 4):

$$\theta_{cl} = \frac{2R_o M^{1/3}}{d_A(1+z)} \quad (10)$$

where a cluster of virial mass $M = 1 \times 10^{15} M_\odot$ has virial radius R_o Mpc at redshift $z = 0$. If we compare Eqns 9 and 10, we can see that both depend only on the redshift and cluster mass (assuming that the other parameters S_o, T_o, f_b and R_o are fixed by local observation). Thus, in principle, measurements of total flux S and apparent size θ_{cl} provide both the cluster mass and redshift.

Fig. 1 contains a plot of the correlation between total flux and apparent size at different redshifts using the model developed above. Each line in this plot represents a single redshift and range of cluster mass between $3 \times 10^{13} h^{-1} M_\odot$ (left) and $1.0 \times 10^{15} h^{-1} M_\odot$ (right). The redshifts are, from top to bottom, $z = 0.05, 0.1, 0.25, 0.5, 0.75, 1, 1.5$. This plot shows clearly that different redshifts are well separated, allowing one to solve for redshift and mass with observations of the total flux and apparent size. The symbols show the case of simulated data. In this case, the clusters do not follow the scaling relations of the previous model. Note that the sizes of the simulated clusters are isophotal sizes rather than virial sizes, because there is no clear observational signature of the virial region in the SZE properties of a cluster.

Both Eqn. 9 & 10 can be solved for mass M . Figure 2 contains a plot of M versus z for specific values of the total flux S (dotted line) and the apparent size θ_{cl} (dashed line). These two functions intersect at the real redshift of the cluster. This intersection along with the measurement of cluster size could be used to produce a probabilistic statement about the cluster redshift. This is illustrated by the solid line in Fig 2, which shows a Gaussian probability distribution for the cluster redshift that reflects the uncertainties in the measured apparent size. These uncertainties are modelled as a function of the spatial resolution of the experiment (FWHM) which introduces an uncertainty in the observed apparent size and consequently on the derived redshift.

3 A METHOD FOR ESTIMATING REDSHIFTS

The arguments outlined in the previous section are idealized. In a real experiment, the situation would depart from that described above for several reasons: (i) clusters do not follow the scaling relations of Eqns. 9 and 10 perfectly, because of departures from equilibrium and variation in cluster structure due to ongoing merging that is quite common (e.g. Mohr et al. 1995), (ii) a real experiment is affected by instrument noise and limited by sensitivity, which limits ones ability to estimate the total flux and apparent size. Estimating cluster redshifts from SZE observations is then a much more complicated task in practice (see symbols in Fig. 1); nevertheless, the underlying scaling outlined in the previous section is expected to be a good description of the cluster population in a statistical sense. Therefore, here we describe an empirical method for estimating redshifts using SZE morphology and calibration through direct redshift measurement in a subsample of the clusters.

In developing this method we are guided by several critical realizations:

- In the ideal case we have assumed that *all* clusters lie perfectly on self-similar scaling relations (Eqns 9 and 10). There are observed scaling relations in the galaxy clusters which connect, for example, X-ray luminosity to temperature and virial mass to temperature. But even in these two well known cases, the scaling relations have an intrinsic scatter, and there is still an ongoing debate about the exact form of these relations. Thus, any redshift estimator that employs scaling relations must allow for scatter and must not require that the exact form of the scaling relation be known.

- Due to noise sources and the limited instrument sensitivity, it will not be possible to observe the entire extent of a cluster. Therefore, it will be difficult to estimate the total flux and size of the cluster from the observed signal. One alternative is to work directly with the observed quantities like the isophotal flux and isophotal size, where the isophote is chosen to lie well above the noise limits of the data. Thus, our method must work with readily available observational quantities.

- X-ray observations indicate that cluster gas distributions can be reasonably well approximated with β -models, but important departures remain (e.g. Mohr et al. 1999). Observations also indicate that clusters are not isothermal (e.g. Markevitch et al. 1998), which is no surprise given the prevalence of merging (and/or temperature gradients). Thus, our method will have to allow for the fact that cluster structure varied significantly from system to system.

- In practice, observations may provide significantly more information than is contained in the isophotal flux or size alone. Therefore, we need to develop a method that can handle multiple observables— even redundant observables— in an optimal and graceful manner.

3.1 SZE Observables

The idea behind morphological redshift estimation is that by combining many observables taken from the 2D SZE cluster profile it is possible to *divide* the clusters in different groups, each one for a different redshift interval. The observables must be such that they take into account the last points of the previous section. The list below is not exhaustive, but it includes all the observables used in the following section in our attempt to estimate cluster redshifts.

- **Isophotal size.** The apparent isophotal size (mean diameter) θ_I is given by the following expression

$$\theta_I = 2\sqrt{A/\pi} \quad (11)$$

where A is the total (apparent) area enclosed by the isophote (Mohr & Evrard 1997). In this work, we will use an isophote defined to be well above the instrument sensitivity. This sensitivity defines a threshold in the 2D images. The X-ray isophotal size exhibits a tight correlation with the emission weighted X-ray temperature both in local samples (Mohr & Evrard 1997) and in intermediate redshift samples (Mohr et al. 2000). Current SZE observations do not have the required sensitivity to examine this property, but many future experiments will have sufficient sensitivity.

- **Isophotal flux.** The isophotal flux is just the total flux within the isophote.

$$S_I = \int_A S(\theta) d\Omega \quad (12)$$

This quantity has never been examined in X-ray observations of ensembles of clusters, but in hydrodynamical simulations this quantity appears to be strongly correlated with the isophotal size. Nevertheless, we include this quantity, because it may provide additional information, and our method handles redundant observables gracefully.

• **Central amplitude.** For the case of the β -model described above the central amplitude is:

$$A_o = B_o r_c n_o T \Phi(0) \quad (13)$$

The central amplitude only depends on the redshift through the intrinsic cluster evolution (z -dependence of r_c , n_o and T). The central amplitude is the integrated effect of the projected electron population through the cluster center. If one assumes the scaling relations given in Eqns 5 and 4, the central decrement is directly proportional to the total cluster mass. The situation will be more complicated in real clusters, but the example of the β -model is useful to illustrate the utility of the central decrement.

• **First and second derivatives of the SZE profile.**

The first and second derivatives of the observed brightness profile for the β -model (see Eqns 7 and 8) are shown in Figure 3, where we also show the projected density profile (proportional to $\Phi(\theta)$) for comparison. The curves have been renormalized by their respective maximums. The core radius in this case was $\theta_c = 0.5$ arcmin, and $p = 10$.

The second derivative evaluated at the cluster center ($\theta = 0$) is

$$\frac{d^2 B(\theta)}{d\theta^2}(0) = -B_o \frac{r_c n_o T}{\theta_c^2} \left(\Phi(0) + \frac{2}{p} \right) \quad (14)$$

which depends on the redshift through the evolution of θ_c . In the regime of interest ($p \gg 2$), the second derivative in the center is a tracer of the core radius.

The first derivative in the center is null for all the clusters, but it is clear in Fig 3 that the first derivative reaches a maximum at $\theta \sim \theta_c$. The position of the maximum coincides with the region where the second derivative vanishes. The value of the first derivative at the core radius is:

$$\frac{dB(\theta)}{d\theta}(\theta_c) \propto \frac{B_o r_c n_o T}{\theta_c} = B_o n_o T d_A \quad (15)$$

That is, the first derivative in the region where the second derivative vanishes is independent of the core radius and is proportional to the angular diameter distance. In cases where the core radius is proportional to the mass, the second derivative in the center and the first derivative in the region where the second derivative vanishes should be useful in breaking the degeneracies between the cluster mass and redshift.

• **Minkowski functionals.** Several recent works have suggested that Minkowski functionals applied to galaxy clusters should be good tracers of the cluster evolution (Beisbart et al. 2001). If clusters form by merging events, their internal structure should evolve with redshift (although local clusters are known to exhibit lots of evidence for merging). Morphological evolution can in principle be traced with Minkowski functionals. In this paper we will consider three of them: (i) total perimeter of the isophote, (ii) ellipticity of the isophote and (iii) number of subgroups above the

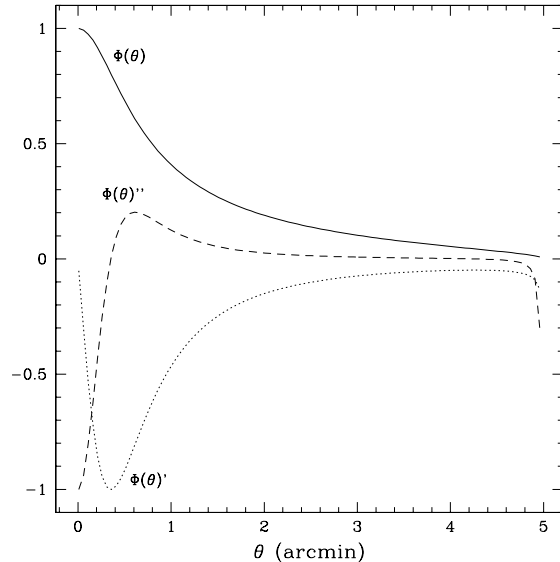


Figure 3. Projected density profile (solid line) as a function of radius. Also shown are the first derivative (dotted line) and the second derivative (dashed line). All curves have been renormalized. The core radius is $\theta_c = 0.5$ arcmin and the ratio between the virial and core radius is $p = 10$.

isophote. In a recent paper employing Minkowski functionals, the authors claim that some evolution with redshift in the ellipticity of galaxy clusters can be observed in large optical and X-ray samples (Plionis 2002).

• **Wavelet coefficients.** The mexican-hat wavelet (MHW) is the second derivative of a Gaussian, and it has been proposed as an ideal filter for compact source subtraction (e.g. Cayón et al. 2000; Vielva et al. 2001). Although the use of the MHW and the number of coefficients (scales) is somewhat arbitrary, we will include them just to show that the inclusion of more observables does not pose problems for this method. We take the 3 MHW coefficients at the center of the cluster, which produces coefficients that are highly correlated with the second derivative. By changing the scale of the MHW we are sampling the cluster at different radii. The three scales considered in this work are $s = 0.25, 0.75, 1.66$ arcmin.

3.2 Principal Component Analysis

Principal component analysis (PCA hereafter) has been widely used in the last years as a powerful classifier of data sets (e.g. Deeming 1964; Teuber et al. 1979; Whitney 1983; Ronen et al. 1999). For our particular case, PCA has several desirable advantages which can be briefly summarized as follows: (i) PCA produces an optimal linear combination of the observables that maximizes the variance of the linear combination (or *projection*), (ii) there is no limit in the number of observables, (iii) it is a *non-parametric method*, which means no assumptions about the cluster scaling relations are required, (iv) the principal components returned by PCA are by definition independent, which simplifies their use in the final computation of

the redshift of the cluster.

In this paper we will give only a brief description of PCA. The reader is referred to the abundant literature about PCA for a more detailed description of the method.

Let us consider a multivariate data set formed by N observations, each observation producing m observables. In our particular case the observations will be the resolved SZE images and the *observables* will be the morphological quantities derived from each one of the images. This data set can be considered as an array of N elements in an space of m dimensions. That is, each observation has m coordinates. Hereafter, we will refer to our data set as the matrix X_{Nm} . The idea of PCA is that, in many cases, it is possible to reduce the dimensionality of the problem without losing any significant amount of information. PCA is specially powerful in those cases where there are correlations between some of the observables. In this case, the dimensionality of the problem is reduced by *projecting* the entire data set over a new orthogonal coordinate system which is aligned with the direction of the main correlations in the \mathbb{R}^m space. The direction of the correlations in \mathbb{R}^m can be found by minimizing the sum of distances between the data points and the direction of the correlation. However, this is equivalent to maximizing the variance of the data points when projected onto the direction of the correlation. This is what PCA does.

Finding the principle components reduces to an eigenvalue problem (eigenvectors and eigenvalues of the covariance matrix $S = X_{Nm} \times X_{Nm}^\dagger$). The information carried out by each one of the principal components (eigenvectors) is proportional to the value of its associated eigenvalue. So, the eigenvector with the highest eigenvalue contains the highest amount of information. On the contrary, the eigenvectors associated with the lowest eigenvalues does not retain much useful information and they can be dominated by the *noise* in the data. One can, therefore, consider only the eigenvectors associated with the highest eigenvalues to *compress* the data set. In our case, the m observables for each cluster will be compressed into p principal components. The criterion to chose the value of p is given by the percentage of the total variance retained by the p highest eigenvalues. Usually a good criterion is to retain only those eigenvalues for which the previous percentage is about 90 – 95%. For this particular application, we will see in the next section how we can retain approximately $\approx 90\%$ of the variance with only the first three principle components. As we will see, our list of observables is highly redundant!

3.3 Redshift estimation

The final component is the probability distribution for the cluster redshift z given the data d . We use Bayes theorem for this purpose;

$$P(z/d) \propto P(z)P(d/z) \quad (16)$$

where $P(z)$ is known as the *prior*; it provides the probability of any cluster to be at redshift z . This prior is cosmologically dependent, and it is in principle well defined if one knows the selection function of the survey. For simplicity, we will consider a constant prior in this work; however, when estimating cluster redshifts in a real survey where a good estimate of the cluster redshift distribution is known (i.e.

$P(z) \propto dN/dz$), this information should also be included when making cluster redshift estimates. The second term, $P(d/z)$, is known as the *likelihood* of the data. In our case, the data are the three principal components. Because these components are orthogonal by construction, we model the likelihood as;

$$P(d/z) = P(pc_1/z)P(pc_2/z)P(pc_3/z) \quad (17)$$

where pc_i is the i^{th} principal component. Each one of this individual probabilities, $P(pc_i/z)$, gives the probability of the observed principal component, pc_i , to be associated with the redshift z .

Computing accurate $P(pc_i/z)$ is absolutely critical, because errors would likely lead to biases in the redshift estimates. The safest approach is a process that we call *self-calibration*, which requires an observed training set of clusters with independently known redshifts. Such a training set could be arranged by simply carrying out a portion of the SZE survey in regions of the sky that have been spectroscopically observed as part of the SDSS or 2dF surveys. At high z , our calibration method will be limited by the availability of identified clusters at those redshifts and a follow up of these clusters will be needed. With measured redshifts for some of the clusters, we can compute $P(pc_i/z)$ for each principal components over a range of redshifts. Here we will model the pdf as a Gaussian with two free parameters, the mean value of the principal component at redshift z , $\overline{pc_i}(z)$, and its dispersion at the same redshift, $\sigma_{pc_i}(z)$. With this form the likelihood for pc_i is

$$P(pc_i/z) = e^{-\frac{(pc_i - \overline{pc_i}(z))^2}{2\sigma_{pc_i}(z)^2}} \quad (18)$$

Other probability distributions (i.e. Poisson, χ^2) could be used, and if the training set were large enough, one could use the histogram (pdf) of the principal components directly.

As a first application of our method, we have applied PCA to the toy model of subsection 3.1 with 5 observables; total flux, total size, central amplitude, first derivative and second derivative. The result is that only the first two resulting principal components are relevant. The first one retains 72.46 % of the total variance and the second one retains 27.53 %. This is not surprising since there are only two independent variables in the toy model (redshift and mass). The first PC is dominated by the two derivatives and the total size while the second PC is dominated by the central amplitude and the total flux. The recovered redshift is unbiased and the errors are small (1 σ error less than 10 %).

4 APPLICATION TO SZE IMAGES FROM HYDRODYNAMICAL SIMULATIONS

In this section we will apply our method to SZE images of simulated galaxy clusters. But first we provide a brief description of the simulations.

4.1 Simulations

The clusters were simulated with a combined dark matter and hydrodynamics code in a cosmological-constant dominated universe ($\Omega_m = 0.3$, $\Lambda = 0.7$, $h = 0.7$, $\Omega_b = 0.026$ and $\sigma_8 = 0.928$). The dark matter was modeled with an

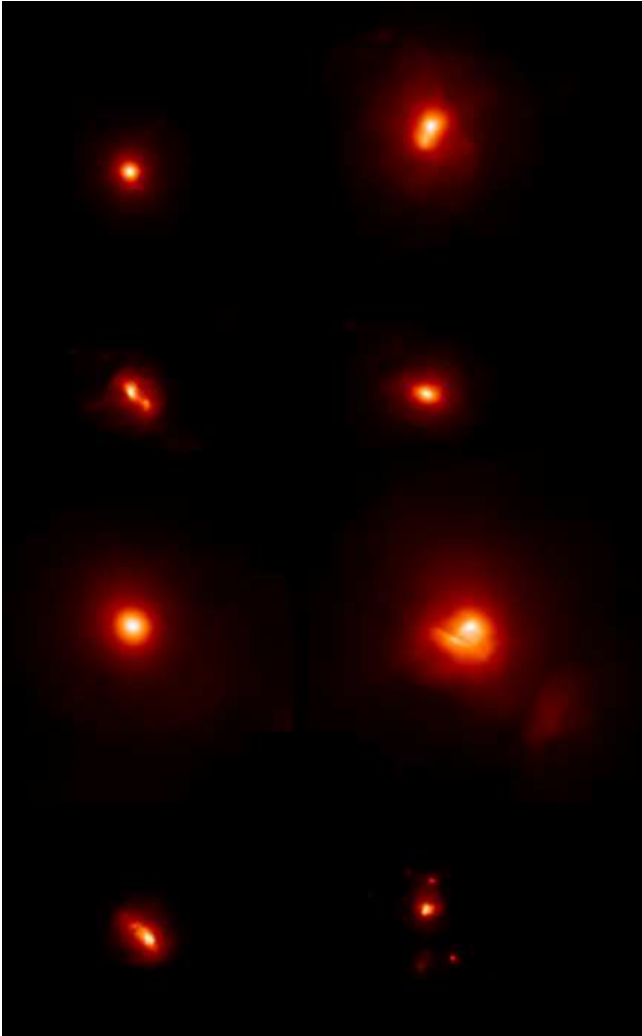


Figure 4. A sample of simulated clusters with different masses and redshifts. From top to bottom. Upper row, two clusters with the same redshift ($z = 0.25$) but different masses. Next row, two clusters with redshifts 0.75 (left) and 0.5 (right) and different masses. Next row, two clusters with the same redshift ($z = 0.1$) but different mass. Bottom row, two clusters with redshifts 1.0 (left) and 1.5 (right) and different masses. The dimension of this image is 80 arcmin in the horizontal direction and 160 arcmin in the vertical direction.

adaptive particle-mesh method, while the gas was followed with an adaptive mesh refinement technique (Bryan 1999; Norman & Bryan 1999). This grid-based method adds additional meshes in high-density regions to obtain high resolution in the central regions of clusters, while low-density regions are simulated at low resolution in order to keep the CPU requirements modest. The best resolution so obtained is 16 kpc, with generally about 100,000 particles within the virial radius of each cluster. The simulations do not include cooling and star formation due to the uncertainty in modelling these processes. This somewhat reduces the realism of the simulations, but because we are only testing the method with the simulated clusters, not calibrating it, this should not affect our conclusions substantially.

Clusters used in this study are taken from a volume-limited, simulated sample and range in mass from 0.7 to

Figure 5. The data set X_{Nm} projected onto the first three principal components. Blue clusters (larger dots) are low redshift ones, red points (smallest size) are highest redshift, green/yellow clusters (intermediate sizes) lie in between (intermediate z).

$2.0 \times 10^{15} M_{\odot}$ at $z = 0$. Maps of the Compton parameter y_c are generated, some of which are shown in Figure 4. The same clusters are imaged at a variety of redshifts, so the various redshift samples are not fully independent (this makes our conclusions conservative in the sense that it should decrease the observed differences and hence make it more difficult to separate the various redshifts than with a real observational sample). The clusters are imaged at the following discrete redshifts, $z = 0.05, 0.1, 0.25, 0.5, 0.75, 1.0$, and 1.5.

4.2 Observations

We filter the images with a Gaussian filter (FWHM 25 arcsec) to simulate the effect of the finite instrument resolution. This resolution is achievable with some current experiments (Pointecouteau et al. 2001), but achieving this resolution is not straightforward. For instance, it requires a single dish antenna of 30 m diameter like IRAM working at ~ 3 mm to achieve this resolution. Interferometers can also produce images with these resolutions. The instrument sensitivity is included by setting a threshold on the filtered Compton parameter images. The sensitivity of the experiment to the SZE signal will depend basically on the instrumental noise and the confusion noise (mainly due to primordial CMB and point sources). The confusion noise can be reduced with multifrequency experiments, which allow partial subtraction of the CMB component. Higher angular resolution observations dramatically reduce the point source noise contribution (easily carried out by existing interferometers with long baselines).

Here we assume that we can see only the cluster emission above a specific threshold that corresponds to $y_c^{th} = 8.0 \times 10^{-6}$. This threshold corresponds to our isophote in the isophotal size and flux. With this threshold, we lose some of the high redshift ($z = 1.5$) clusters, which after filtering have a surface brightness below the threshold, but we can still observe most of our simulated high- z clusters.

Our data set X_{Nm} is then a matrix with a number of rows, N , equal to the number of observed clusters in the survey, and a number of columns, $m = 11$, equal to the number of observables for each cluster. When using PCA, it is convenient to re-scale the observables in order to make them of the same order of magnitude. Here we use the \log of the observables and then solve for the principle components of the covariance matrix, $S = X_{Nm} \times X_{Nm}^{\dagger}$. We find that the first three principle components are responsible for $\approx 90\%$ of the dispersion in our data. That is, 3 principle components contain almost all the information within our 11 original observables.

Table 4.2 contains the first three eigenvectors with their associated eigenvalues (λ) and percentages. The form of the eigenvectors clearly shows which of the 11 observables are the most relevant. The first principal component (with the highest eigenvalue), PC1, is dominated by the isophotal flux,

	PC1	PC2	PC3
λ	5.15	3.56	1.03
Percentage	46.8	32.4	9.4
Observables	Eigenvectors		
Isoph. Flux	-0.97	-0.21	-0.04
Isoph. Size	-0.98	-0.11	-0.05
Central Amp.	-0.38	-0.88	0.01
∂^2	0.75	-0.62	-0.03
∂	0.81	-0.47	0.07
perimeter	-0.97	-0.11	-0.16
ellipticity	0.18	-0.2	-0.66
N_{groups}	0.21	-0.1	-0.74
MHW1 (0.25)	0.62	-0.76	-0.02
MHW2 (0.75)	0.07	-0.96	-0.02
MHW3 (1.66)	-0.65	-0.71	-0.01

Table 1. First 3 eigenvectors of the principle component analysis (columns) and associated eigenvalues (first row) of the 11 observables outlined in §4.2. The numbers in parenthesis are the typical scales of the MHW’s in arcmin. The second row gives the associated percentage for each one of the eigenvectors. The principal components are each a linear combination of the observables; the coefficients of the combination are listed.

the isophotal angular size, the perimeter and the first derivative. The second principal component is dominated by the central amplitude, the MHW coefficients and the second derivative and the third principal component is dominated by the ellipticity and the number of subgroups. It is not surprising to see that the flux and size are contributing significantly to the most relevant principal component (PC1). On the contrary, the ellipticity and number of subgroups only contribute significantly to the third principal component.

In Figure 5 the data set is projected in the space of the three principal components. We have used a *spectral* scale of colors. That is, blue points are clusters at low redshift, green and yellow points are intermediate redshift and red points are high redshift. As can be seen, different redshifts are *grouped* in different regions in this 3D space. This will allow us to discriminate between low, intermediate and high redshift clusters. Figure 6 contains the projection of the original data set in the space defined by the first and second principal components only. The different grouping of clusters as a function of their redshift can be also appreciated in this space.

To estimate the redshift we use the expression given in Eqn. 17, which requires the quantities $\overline{pc_i}(z)$ and $\sigma_{pc_i}(z)$ which must be estimated from the training set. In our case the simulated clusters lie at discrete redshifts ($z = 0.05, 0.1, 0.25, 0.5, 0.75, 1.0$, and 1.5), and so we compute $\overline{pc_i}(z)$, and $\sigma_{pc_i}(z)$ only at those redshifts. A number of clusters > 10 per redshift interval is needed in order to properly estimate $\overline{pc_i}(z)$, and $\sigma_{pc_i}(z)$. The total number of clusters in our simulations is ≈ 100 and there are about 10–15 clusters

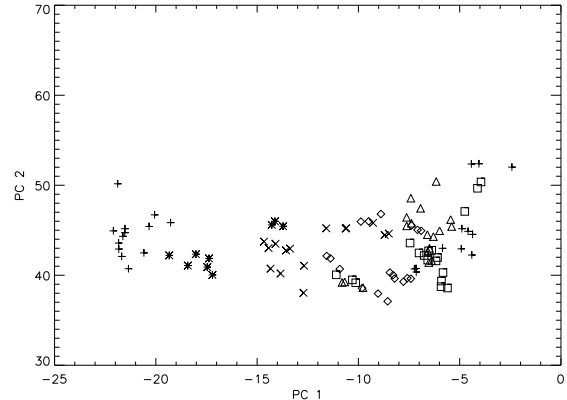


Figure 6. Projection in the first and second principal components space. (+)’s are for $z = 0.05$, (*)’s for $z = 0.1$, (x)’s for $z = 0.25$ diamonds for $z = 0.5$, triangles for $z = 0.75$, squares for $z = 1.0$ and (+)’s again for $z = 1.5$.

at each one of the discrete redshifts. Due to this low number of clusters, we have taken the training set to be coincident with the total sample of clusters. Since we have discrete redshifts in our simulation, we have to interpolate $\overline{pc_i}(z)$ and $\sigma_{pc_i}(z)$ for arbitrary redshift. In a real survey the situation could be much better if redshifts were available for a larger number of clusters with a more continuous distribution in z . Then, the training set could be larger and without any need of interpolation.

Once we have $\overline{pc_i}(z)$, and $\sigma_{pc_i}(z)$ for different redshifts we can apply the Bayesian estimator (see Eqn. 17) for each one of the remaining clusters. Figure 7 shows the final result of our method. The mean of the recovered redshifts follows very well the true redshift of the clusters. The error bars are small at low redshifts but they grow larger at higher redshift. We also show the result obtained when only the first principal component is considered in the analysis (point at $z = 0.05$ is not shown). In this case, the error bars and bias are smaller at the high redshift interval but they are larger at the smaller redshifts. If we look at Figure 6 and we project the points into $PC1$ and $PC2$ we see how the projection into $PC2$ is more *noisy* in the sense that the overlap of the different redshift intervals is stronger than in the projection into $PC1$. This overlap affects the individual likelihoods (Eq. 18), which can show a bimodal or trimodal behaviour specially at high redshift (i.e. the individual likelihood for $PC2$ (and $PC3$) has local maxima at different redshifts). The addition of the second and third principal components in the analysis adds *noise* to the z -estimation in particular in the high redshift interval. On the contrary, at low redshifts, the second and specially the third principal component (see Figure 5) show a clear dependence with the redshift which helps to better estimate z . Consequently the redshift estimation becomes more noisy when we include the second and third principal components at high redshift but, in the low- z interval, the second and third principal components helps to reduce the error bars.

To understand this behaviour, it is helpful to study how different observables contribute to the redshift estimation. We have split the list of observables into two groups and applied PCA to each group. In the first group we include three of

the most relevant observables, central amplitude, isophotal flux, and isophotal size while in the second group we include the remaining 8 observables, first and second derivatives, 3 MHW coefficients, ellipticity, number of subgroups and perimeter. We compare the results in Figure 8. The first group renders a z -estimation similar to the case where only PC1 is used in the analysis (see Figure 7). This is not quite surprising since PC1 was dominated by the isophotal flux and isophotal size. This result shows that even with a small number (3) of observables it is possible to get an estimate of the redshift. However, the other observables also contain information about the redshift. This is also illustrated in Figure 8 (dotted line). In this case it is important to note how the 8 additional observables help to reduce the scatter in the low redshift interval. Thus it can be useful to include more observables in the analysis to reduce the uncertainty. However, the additional 8 observables increase the scatter at higher redshifts.

Our results show that morphological redshifts are not *precise* estimators of the cluster redshift, but they are useful providing a first guess that could be critical in planning the cluster followup observations to determine photometric or spectroscopic redshifts. Also, we note that the redshift distribution expected for cluster surveys does not contain any sharp features in redshift, suggesting that even moderately accurate redshifts like those possible with morphological estimators may be sufficient for deriving cosmological constraints. This clearly deserves further attention.

5 CONCLUSIONS

We have developed a means of estimating galaxy cluster redshifts using only observed SZE properties of the clusters. Using a toy model we show how morphological quantities associated to clusters may contain redshift information. We also show how modelling of the morphological quantities can lead to systematic errors in the redshift estimation. We then propose an alternative method which is model independent. Specifically, we have combined several redshift sensitive SZE observables using a standard principal component analysis (PCA). The PCA led to significant compression, showing that most of the redshift information contained in the 11 SZE observables can be expressed in three orthogonal linear combinations. The use of the PCA has several advantages. These include (i) no required assumptions about cluster scaling relations, (ii) straightforward to use of direct observables (like the isophotal quantities), and (iii) orthogonality of the principal components. The method must be *calibrated*, and we suggest using a cluster training set that has redshift estimates from photometric or spectroscopic means. This training set is required to build the likelihoods of the principal components as a function of redshift.

In our analysis we include 11 different *observables*: isophotal flux, isophotal size, central amplitude, second derivative at the center, the mean of the first derivative in the region where the second derivative vanishes, the ellipticity and perimeter of the isophote, the number of subgroups above the isophote, and three Mexican-hat wavelet coefficients evaluated at the cluster center. Principle components were determined, and the first three components had ≈ 90

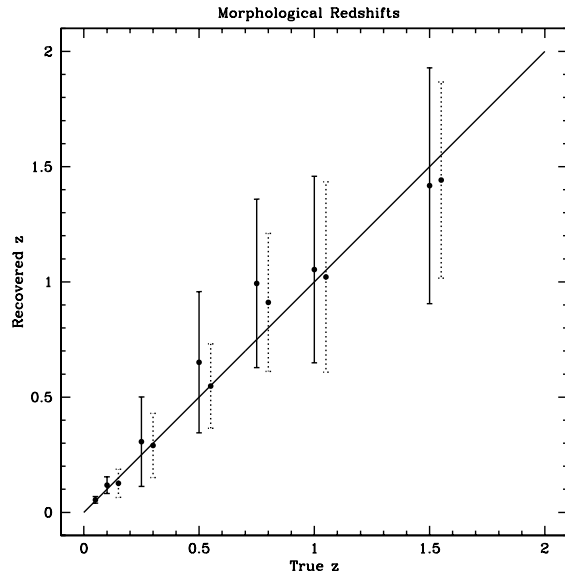


Figure 7. Mean recovered redshift and error bar (dispersion) as a function of redshift. The solid line represents the ideal situation where the recovered redshift equals the true one. For comparison we also show the corresponding recovered redshifts when only the first principal component is used in the Bayesian approach (dotted error bars). The error bars for this case have been displaced 0.05 units in redshift to the right.

% of the variance of the data. Application of our redshift estimator using these three components indicates that the method can distinguish between clusters at low, intermediate and high redshift.

Although the error bar for a specific cluster redshift is fractionally large, our method should be useful for future SZE surveys, providing a preselection of low, intermediate and high redshift clusters. This preselection can be used to optimize the optical followup. Because of the smoothly varying nature of the cluster redshift distribution expected in future surveys, it may also be possible to obtain cosmological constraints directly with these morphological redshifts. As shown in Fan & Chiueh (2001), the ratio of the number of clusters above and below a given redshift can be a useful cosmological discriminator. This kind of analysis could be well suited to our morphological redshift estimates.

A requirement for morphological redshifts is resolved, SZE cluster images. Our estimates were carried out assuming an instrument resolution of 25 arcsec. This resolution requirement makes our method inappropriate for application to clusters detected in the *Planck* Surveyor mission, but there are several planned interferometric and single dish SZE surveys which could take advantage of our method.

Although in this work we have only considered the case of the SZE, our method can be extended to X-ray and optical cluster surveys. The main difference would be that the flux in the X-ray and optical bands are inversely proportional to the luminosity distance squared and the region of the spectrum observed by a particular instrument also varies with redshift. The difference between the luminosity distance and the angular diameter distance is a factor $(1+z)^2$. In general, the X-ray and optical flux is much more sensitive to the

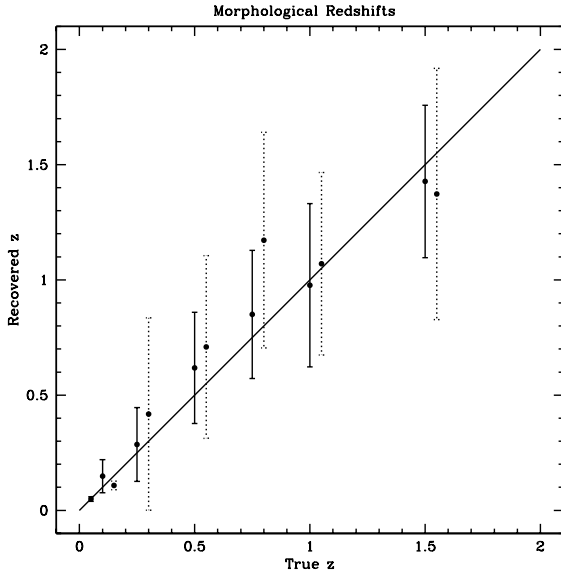


Figure 8. Recovered vs true redshift in the case where only three observables: central amplitude, isophotal flux, and isophotal size are considered in the PCA analysis (solid line). This result is comparable with what the one obtained when the 11 observables are considered but only the first PC was used in the redshift estimation. The dashed lines show the corresponding redshift estimation when the remaining 8 observables are considered in the analysis (first and second derivatives, 3 MHW coefficients, ellipticity, number of subgroups and perimeter) and the central amplitude, isophotal flux, and isophotal size are excluded. The true redshift has been displaced 0.05 to the right to avoid overlapping. Note the good constraints on z obtained by these eight observables at low z .

cluster redshift than is the SZE flux. Although the redshift of galaxy clusters in X-rays can be obtained, for some clusters, directly from their X-ray spectrum (with typical errors of $\Delta z \approx 0.2$), for many clusters with a low SNR the redshift can not be obtained from this method. Large, planned X-ray surveys will have a preponderance of low signal to noise detections, making the use of morphological redshifts (alone or combined with photometric redshifts) very promising.

ACKNOWLEDGMENTS

This research has been supported by a Marie Curie Fellowship of the European Community programme *Improving the Human Research Potential and Socio-Economic knowledge* under contract number HPMF-CT-2000-00967. JJM acknowledges financial support from the NASA Long Term Space Astrophysics grant NAG 5-11415.

REFERENCES

- Bahcall N. A., Fan X., 1998, *ApJ*, 504, 1
 Bahcall N. A., Fan X., Cen R., 1997, *ApJ Letters*, 485, L53
 Beisbart C., Valdarnini R., Buchert T., 2001, *A&A*, 379, 412

- Borgani S., Rosati P., Tozzi P., Stanford S. A., Eisenhardt P. R., Lidman C., Holden B., Della Ceca R., C. N., Squires G., 2001, *ApJ*, 561, 13
 Bryan G. L., 1999, *Computing in Science and Engineering*, 1:2, 46
 Bryan G. L., Norman M. L., 1998, *ApJ*, 495, 80
 Cavaliere A., Fusco-Femiano R., 1978, *A&A*, 70, 677
 Cayón L., Sanz J. L., Barreiro R. B., Martínez-González E., Vielva P., Toffolatti L., Silk J., Diego J. M., Argüeso F., 2000, *MNRAS*, 315, 757
 Deeming T. J., 1964, *MNRAS*, 127, 493
 Diego J. M., Martínez-González E., Sanz J. L., Benítez N., Silk J., 2002, *MNRAS*, 331, 556
 Diego J. M., Martínez-González E., Sanz J. L., Cayón L., Silk J., 2001, *MNRAS*, 325, 1533
 Eke V. R., Shaun C., Frenk C. S., 1996, *MNRAS*, 282, 263
 Eke V. R., Shaun C., Frenk C. S., Henry P. J., 1998, *MNRAS*, 298, 1145
 Fan Z., Chiueh T., 2001, *ApJ*, 550, 547
 Grego L., Carlstrom J. E., Reese E. D., Holder G. P., Holzappel W. L., Joy M. K., Mohr J. J., Patel S., 2001, *ApJ*, 552, 2
 Haiman Z., Mohr J. J., Holder G. P., 2001, *ApJ*, 553, 545
 Henry J. P., 2000, *ApJ*, 534, 565
 Holder G., Haiman Z., Mohr J. J., 2001, *ApJ Letters*, 560, L111
 Jones C., Forman W., 1984, *ApJ*, 276, 38
 Majumdar S., Mohr J., 2002, *ApJ Letters*
 Markevitch M., Forman W. R., Sarazin C. L., Vikhlinin A., 1998, *ApJ*, 503, 77
 Mathiesen B. F., Evrard A. E., 1998, *MNRAS*, 295, 769
 Mohr J. J., Evrard A. E., 1997, *ApJ*, 491, 38
 Mohr J. J., Evrard A. E., Fabricant D. G., Geller M. J., 1995, *ApJ*, 447, 8+
 Mohr J. J., Mathiesen B., Evrard A. E., 1999, *ApJ*, 517, 627
 Mohr J. J., Reese E. D., Ellingson E., Lewis A. D., Evrard A. E., 2000, *ApJ*, 544, 109
 Norman M. L., Bryan G. L., 1999, in *ASSL Vol. 240: Numerical Astrophysics Cosmological Adaptive Mesh Refinement* {CD}. pp 19+
 Plionis M., 2002, *ApJ Letters*, 572, L67
 Pointecouteau E., Giard M., Benoit A., Désert F. X., Bernard J. P., Coron N., Lamarre J. M., 2001, *ApJ*, 552, 42
 Ronen S., Aragon-Salamanca A., Lahav O., 1999, *MNRAS*, 303, 284
 Teuber D. L., Reichmann E. J., Wilson R. M., 1979, *A&A*, 80, 218
 Vielva P., Barreiro R. B., Hobson M. P., Martínez-González E., Lasenby A. N., Sanz J. L., Toffolatti L., 2001, *MNRAS*, 328, 1
 Weller J., Battye R., Kneissl R., 2001, *astro-ph* (0110353)
 Whitney C. A., 1983, *A&A Supp.*, 51, 443

This paper has been typeset from a \LaTeX file prepared by the author.

This figure "Figure5.gif" is available in "gif" format from:

<http://arxiv.org/ps/astro-ph/0207353v2>